



저작자표시-비영리-변경금지 2.0 대한민국

이용자는 아래의 조건을 따르는 경우에 한하여 자유롭게

- 이 저작물을 복제, 배포, 전송, 전시, 공연 및 방송할 수 있습니다.

다음과 같은 조건을 따라야 합니다:



저작자표시. 귀하는 원저작자를 표시하여야 합니다.



비영리. 귀하는 이 저작물을 영리 목적으로 이용할 수 없습니다.



변경금지. 귀하는 이 저작물을 개작, 변형 또는 가공할 수 없습니다.

- 귀하는, 이 저작물의 재이용이나 배포의 경우, 이 저작물에 적용된 이용허락조건을 명확하게 나타내어야 합니다.
- 저작권자로부터 별도의 허가를 받으면 이러한 조건들은 적용되지 않습니다.

저작권법에 따른 이용자의 권리는 위의 내용에 의하여 영향을 받지 않습니다.

이것은 [이용허락규약\(Legal Code\)](#)을 이해하기 쉽게 요약한 것입니다.

[Disclaimer](#)

Ph.D. Dissertation of Medicine

Failure analysis for 3D-printed  
Ti-6Al-4V tumor prosthesis  
– based on mechanical experiments of  
3D-printed metal specimens –

3D 프린팅 Ti-6Al-4V 종양 임플란트 파손분석  
– 3D 프린팅 금속 시편 시험을 바탕으로 –

February 2022

Graduate School of Medicine  
Seoul National University  
Orthopaedic Surgery Major

Park, Jong Woong

Failure analysis for 3D-printed  
Ti-6Al-4V tumor prosthesis  
– based on mechanical experiments of  
3D-printed metal specimens –

Kim, Han-Soo

Submitting a Ph.D. Dissertation of  
Medicine

October 2021

Graduate School of Medicine  
Seoul National University  
Orthopaedic Surgery Major

Park, Jong Woong

Confirming the Ph.D. Dissertation written by

Park, Jong Woong

January 2022

Chair	Lee, Young Ho	(Seal)
Vice Chair	Kim, Han-Soo	(Seal)
Examiner	Hong, Sung Hwan	(Seal)
Examiner	Han, Ilkyu	(Seal)
Examiner	Seo, Sung Wook	(Seal)

# Abstract

## Introduction:

Limb salvage surgery is a mainstay of treatment for bone sarcoma. Due to its random anatomical location, size, and shape, bone sarcoma leaves different bone defects in each patient after tumor resection. Recently, limb salvage surgery using a 3D-printed custom-made Ti-6Al-4V implant has been reported with promising short-term surgical results in orthopedic oncology. However, experimental evidence of the 3D-printed implant's performance and custom-made design efficacy is lacking. After successfully performing a tensile test as a basic test on the Ti-6Al-4V, it became possible to evaluate the performance of other 3D-printed implants that are designed differently each time by using computer-aided analysis of the data obtained from the preceding basic tests.

## Research Method:

The fracture analysis of an implant in a patient who experienced implant failure was conducted with a metal tensile test and computer simulation using a multi-step procedure. First, a tensile specimen was fabricated using an electron beam 3D printer under the same conditions as for producing an implant. Tensile specimens were fabricated with a solid body structure and a mesh structure. Next, tensile tests were performed on these structures to obtain the physical properties of the 3D printed Ti-6Al-4V metal. The fracture surfaces of the implant and 3D-printed tensile specimens were then examined with a scanning electron microscope. Finally, the structure and performance of the implant were analyzed through finite element analysis using this data.

### Result:

As a result of the 3D-printed Ti-6Al-4V specimen experiment, the mesh structure showed a yield strength of 33–54 MPa, and the rigid structure showed a yield strength of 976–1000 MPa. In particular, the elongation of the mesh structure was less than 1%, indicating that it was brittle. In the fracture analysis of the implant and tensile specimens, unmelted metal powders were commonly observed. Following computer simulation of implant performance using the preceding experimental data in a patient-specific human model, a weakness in the upper part of the implant was identified in the normal, fast gait condition.

### Conclusion:

Mechanical properties of Ti6Al4V fabricated by the EBM 3D printer was sufficient for orthopedic implants, compared to those by traditional fabrication. The results of the implant performance analysis using the preceding experimental data and computer simulation predicted the implant fracture site and fracture conditions well. To generalize and simplify analysis of the computer-aided engineering including a human body simulation and FEA, the method needs to be validated with various implants in the future.

**Keyword :** sarcoma, bone malignancy, failure analysis, 3D printing, titanium alloy implant, electron beam melting

**Student Number :** 2018-39923

# Table of Contents

Chapter 1. Introduction .....	1
Chapter 2. Body .....	4
Chapter 3. Conclusion .....	23
Bibliography .....	24
Abstract in Korean.....	32

# Chapter 1. Introduction

## 1.1. Study Background

3D printing is an important manufacturing technology used to fabricate objects with a mesh shape in a single process for the adhesion of various materials [1–3]. Owing to the benefit of the customizable mesh shape fabrication method, the 3D printing process has been widely applied in practical medical research, from customized artificial organs to teeth and bones [4–16]. In the practical orthopedic surgery field, metal 3D printing is more often utilized. In particular, metal implants to replace bone tissue can be manufactured relatively easily, as these are solid. Orthopedic 3D–printed implants are often constructed using the electron beam melting (EBM) process, which imparts desirable mechanical properties to the fabricated implants by printing at relatively high temperatures [17, 18]. Malignant bone tumors of the extremities constitute a life–threatening condition, and functional limb disability may occur even if the patient survives. The key treatment for localized malignant bone tumors is to surgically remove the tumor with wide margins, which involves excising the normal tissue surrounding the tumor. This tumor removal procedure, known as wide excision, often results in severe bone and soft tissue defects.

Reconstructive surgery is performed to minimize the functional deficit after wide excision in a process known as limb salvage surgery. The bone tissue is commonly replaced using conventional modular–type metal implants (endoprostheses) [19–21]. During endoprosthesis implementation, when the remaining normal bone is small after wide excision of the bone tumor, the adjacent joint that has not been affected by the tumor may be sacrificed to fix the implant. Nevertheless, preserving natural joints is highly beneficial for proper joint function and longevity [22,23]. In this regard, joint preservation can be realized by using a personalized implant for the patient, thereby minimizing functional loss.

Although the concept of a patient–customized implant is not new, it has been promoted with the advancement of additive manufacturing (AM). In general, personalized implants fabricated through metal casting cannot be widely applied owing to the associated high cost and considerable production time. A customized implant for use in bone cancer patients should not take too long to fabricate, to avoid excessive tumor progression before surgical treatment. A personalized titanium alloy implant can be fabricated through 3D printing in approximately three weeks [24]. Many researchers have reported promising surgical results for limb salvage operations using 3D–printed customized metal implants made of Ti–6Al–4V [25–27]. However, certain concerns remain with respect to the lack of long–term clinical outcome and experience data. Since sufficient time must elapse to evaluate long–term surgical results, it is critical to thoroughly investigate cases of mechanical failure to enhance implant design and quality.

Uncertainty about 3D–printed implant performance stems from the new manufacturing method itself and the untested custom–made implant designs. Moreover, the time limitation that is given for implant design, validation, and fabrication is often within a few weeks, from cancer diagnosis to limb salvage surgery. To solve this problem, finite element analysis (FEA) for the custom–made implant design should be utilized. However, physical properties, such as the modulus of elasticity and the Poisson ratio of the elements constituting the implant, are required as a prerequisite for using it. Even for a solid structure, the product fabricated by metal 3D–printing lacks performance verification, and little is known about the mesh structure.

## 1.2. Purpose of Research

In this study, the mechanical properties of the solid and mesh structures, which were fabricated by EBM type 3D–printing, were investigated using tensile experiments. Using the preceding experimental data, FEA for a representative implant, which had been used for limb salvage surgery and was broken 6 months postoperatively, was performed. Afterward, the prediction of the implant fracture site and timing through FEA was verified by comparing them with an actual fracture situation.

# Chapter 2. Body

## 1.1. Materials and Methods

### – *3D-printed custom-made implant fabrication*

The mainstay of the treatment for bone malignancy is limb salvage surgery, which is surgery that includes tumor removal with a sufficient normal tissue margin and reconstruction for the resulting bone and soft tissue defect. One of the surgical indications for using a 3D-printed custom-made implant is to save the adjacent joint. For example, as shown in Fig. 1, the right distal femur of the patient contained a malignant tumor, while the nearby knee joint bone was healthy. For the preservation of the natural joint, rather than using a commercial standardized implant, a customized 3D-printed titanium implant was planned for intercalary replacement. For the surgery to be successful, the implant had to meet three major requirements: (1) a hybrid structure with a suitable proportion of mesh for muscle bonding and a solid area for the protection of neurovascular structures from adhesion or scratches, (2) strength to withstand repeated long-term physiological loading, and (3) conformity with other body elements to act as living bone tissue. The schematic diagram of the implant development, which adhered to the major requirements of an artificial implant, and the surgery are illustrated in Fig. 1. The process was conducted as follows: step 1, bone cancer in the local area of the long bone was accurately diagnosed; step 2, the morphology of the cancer-affected bone was designated for removal, while maintaining the natural knee joint; step 3, 3D graphical prototyping was performed to match the empty bone area with a mesh and solid hybrid structured implant; step 4, EBM and post-processing for biocompatibility were performed to fabricate the Ti-6Al-4V implant; and step 5, limb salvage surgery was

performed using the printed/post-processed Ti-6Al-4V implant with proximal and distal fixation at the bone defect following wide excision.

The custom-made implant was manufactured using an EBM type 3D printer (ARCAM A1, Arcam AB, Sweden). The material used for the implant was Ti-6Al-4V alloy powder (Arcam AB, size 45–106  $\mu\text{m}$ ), with a mesh body (lattice) containing a Dode-Thin structure. The process conditions were as follows: electron beam power of 50–3000 W, scan speed of 4530 m/s, and layer thickness of 50  $\mu\text{m}$ .

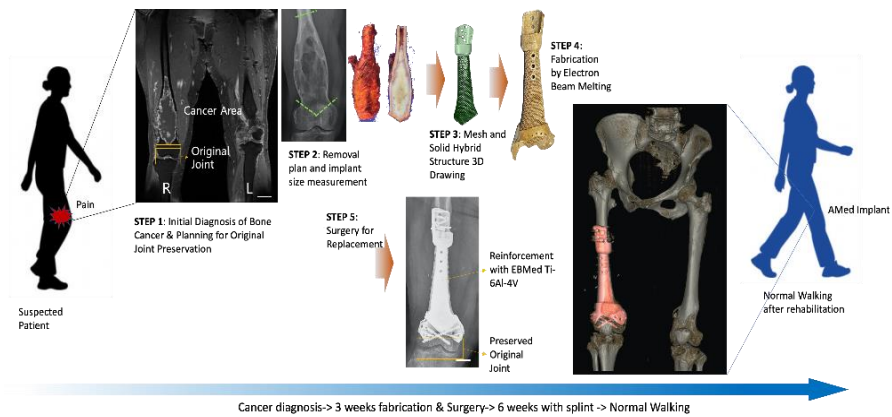


**Fig. 1** Surgical procedure of bone tumor removal with an additively manufactured Ti-6Al-4V implant. Step 1: Initial diagnosis of bone cancer and surgery planning for original joint preservation. Step 2: Cancer removal plan and implant size measurement. Step 3: Design of artificial implant with mesh and solid hybrid structure. Step 4: EBM process with Ti-6Al-4V. Step 5: Surgery to embed the electron beam-melted Ti-6Al-4V implant into the area of the removed cancerous bone, and suturing.

– *Tensile experiment*

The tensile specimens were fabricated under the same conditions as the custom-made implant. To evaluate the mechanical properties under these process conditions, the tensile specimens were fabricated according to the ASTM-E8/E8M standard (round-type and plate-type). The round-type specimens featured a length, diameter, and gauge length of 140, 12.5, and 50 mm, respectively, and the plate-type specimens had a length, width, and thickness of 200, 25, and 6 mm, respectively.

Round-type tensile specimens printed in the XY-H direction and the Z-axis direction were designed to measure the strength of the Ti-6Al-4V alloy fabricated with the EBM 3D printer. The specimens were fabricated with perpendicular building axes (X and Z-axis). The XY-H axis specimens were built along the XY plane. The side with the longest length was placed on the XY plane as the height along the Z direction. The Z-axis specimens were fabricated along the Z direction where the longest side was placed on the Z-axis (Fig. 2a-c).

To investigate the mechanical behavior of the mesh structure, the Dode-Thin type structure was applied along the gauge length of the plate-type specimens. The unit size of the mesh structure was 2 mm. Because the mesh structure had its own axis, two types of mesh structures were configured to 0° and 45° (Fig. 2d, e). All specimens were 3D-printed five by type.

Tensile tests were performed using a universal test machine (Minos-100, MTDI) with a load cell capacity of 100 kN under quasi-static conditions, and a displacement control velocity of 3 mm/min. The corresponding microstructures were analyzed by the electron backscatter diffraction (EBSD) technique, and the aggregation formation and tensile deformation behavior were subsequently studied. The EBSD analysis was conducted using a field emission scanning electron microscope (MIRA I LMH) with a power of 20 kV and step size of 0.5  $\mu\text{m}$ .

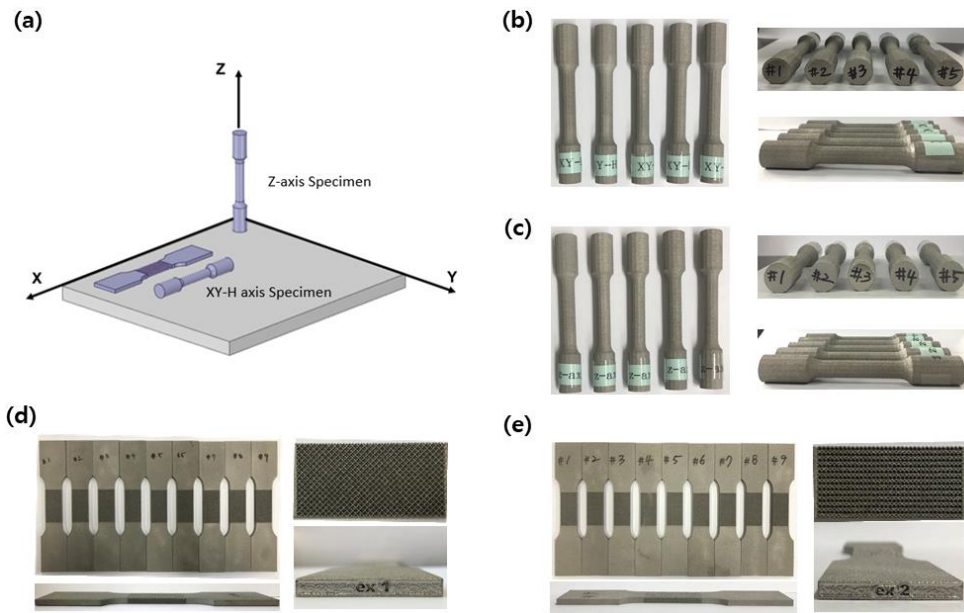


**Fig. 2** Tensile test specimens. a Building axis, b Solid with XY-H axis, c Solid with Z-axis, d Mesh (2 mm Dode-Thin) with XY-H axis, e Mesh (2 mm Dode-Thin rotated to 45°) with Z-axis.

– *Fractography*

The effects of the micropores, unmelted powder, and lack of fusion pores on the tensile behavior were examined by performing a tensile fracture surface analysis with scanning electron microscopy (SEM). To analyze the fracture surface of the 3D-printed Ti-6Al-4V, fractured surface of the implant was examined with SEM. The results of fractography for tensile specimens and fractured implant were compared.

– *Finite element analysis*

To predict the behavior of the 3D-printed implants, FEA was performed. The mechanical properties for the finite elements, which were generated by breaking down the entire structure into sufficiently small, but calculable pieces, were substituted for the

results obtained from the preceding tensile experiments. The boundary conditions, including the direction and magnitude of the external forces, which applied to the implant in the FEA, were derived from a personalized body model using commercial software (AnyBody Modeling System, Denmark).

– *Representative patient with a fractured implant*

To validate the concept of replacing performance evaluation experiments with FEA, a representative patient was selected. The patient experienced extreme clinical consequences of implant fracture 6 months postoperatively.

The representative patient was a 69-year-old woman diagnosed with chondrosarcoma in the left distal half of the femur without distant metastasis. Of note, she had a limb length discrepancy of 10 cm due to a childhood history of osteomyelitis in the distal portion of the contralateral femur (Fig. 3). The patient underwent limb salvage surgery using a 3D-printed customized implant for the distal part of her right femur, with retention of the natural knee joint, and acute shortening of the right femur was performed for partial correction of the limb length discrepancy.

Using the 3D printed Ti-6Al-4V implant, the patient was able to walk independently using her natural knee joint and resume living a normal life six weeks of recovery. Moreover, the leg length discrepancy was partially corrected; thus, postoperative walking was more comfortable for the patient than preoperative walking because both heels touched the ground while standing and walking after the surgery [28,29].

However, as shown in Fig. 3, due to a mild fall at 6 months post-surgery, the Ti-6Al-4V implant fractured at the junction between the implant body and the proximal fixation plate. The implant fracture could be clearly seen in the 3D computed tomography reconstruction and X-ray images, depicted in Fig. 4.

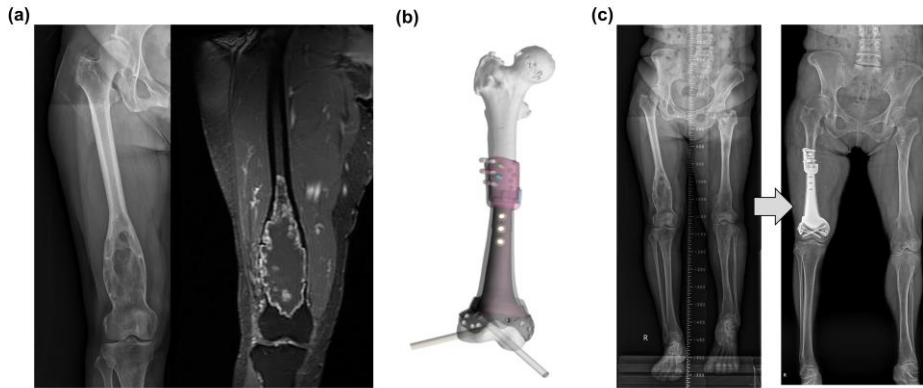


**Fig. 3** Images of a 69-year-old woman as the representative patient. A plain radiography and magnetic resonance imaging results, b Implant design, c Pre- and postoperative teleradiography.

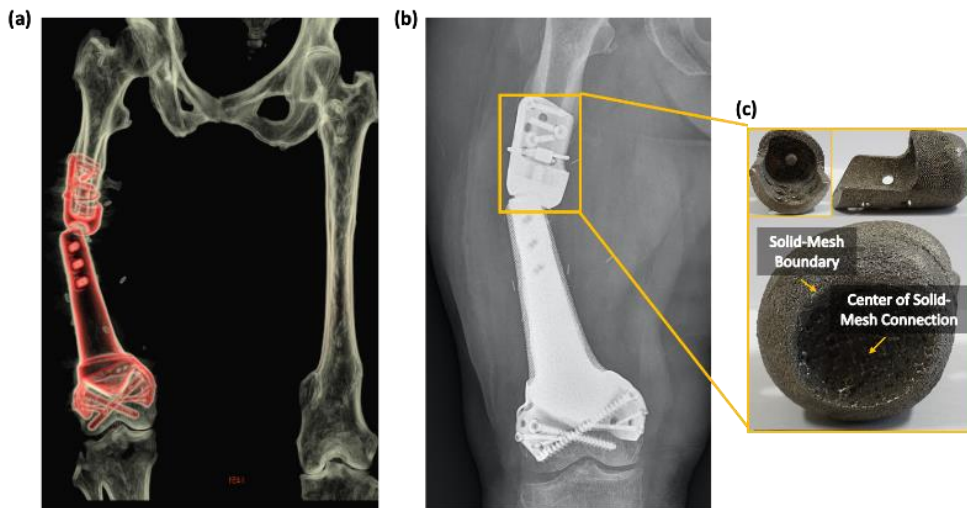


**Fig. 4** Fracture of Ti-6Al-4V implant 6 months post-surgery. a Computed tomography reconstruction image, b Plain radiography image, c Fractured head of the implant (fractured solid-mesh boundary area and fractured center area of solid-mesh connection)

## 1.2. Results

### – Tensile test

The stress–strain curves of the tensile specimens manufactured using the EBM 3D printer indicated that both types of mesh specimens were destroyed without reaching the plastic deformation stage. As indicated in Table 1 and Fig. 5, the yield strengths of the mesh–type specimens were only 33 and 54 MPa, while the yield strengths of the solid–type specimens ranged from 976 to 1003 MPa. Of note, for two types of mesh specimens (ex1: 2 mm Dode–Thin and ex2: 2 mm Dode–Thin rotated to 45°), results and graphs were shown only two specimens with stable stress–strain graphs. In the remaining mesh specimens, stable graphs could not be obtained due to the brittleness of them.

**Table 1.** Tensile tests for the ASTM–E8 standard specimen

Specimen ID	Yield strength (MPa)	Tensile strength (MPa)	Elongation (%)
ex1 #1	33	47	0.7
ex2 #1	54	55	0.2
<i>XY</i> –H #1	1000	1044	7.3
<i>XY</i> –H #2	976	1018	3.9
<i>XY</i> –H #3	980	1028	8.2
<i>XY</i> –H #4	1003	1041	7.9
<i>XY</i> –H #5	977	1018	7.6
<i>Z</i> –axis #1	992	1039	8.8
<i>Z</i> –axis #2	995	1040	9.1
<i>Z</i> –axis #3	1000	1041	11.0
<i>Z</i> –axis #4	1001	1038	7.7
<i>Z</i> –axis #5	986	1027	7.1

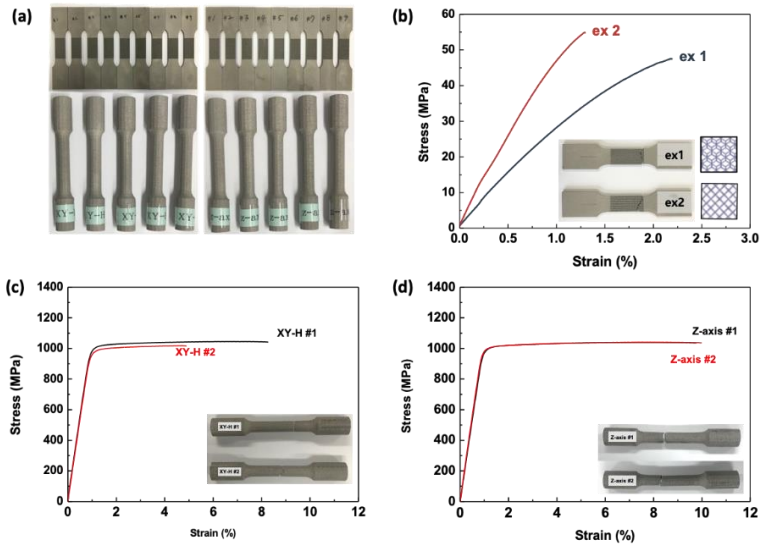


**Fig. 5** Characterization of the mechanical properties of the EBM 3D-printed Ti-6Al-4V specimen. a ASTM-E8 standard (round-type and plate-type) specimens, b Stress-strain curve of the mesh-type specimen, c Stress-strain curve of the round-type specimen (built along the XY plane), d Stress-strain curve of the round-type specimen (built along the Z-axis)

To verify the main reason for such poor elongation of the mesh-type specimen, microstructural analysis was conducted for both the solid- and mesh-type specimens for comparison. Fig. 6 shows the microstructures of the XY-H and Z-axis solid-type specimens. In the figure, typical Widmanstätten microstructures can be observed with lamellar and colony structures, and their texture is developed along the building direction. Thus, owing to their perpendicular orientation, the XY-H and Z-axis specimens naturally exhibited (111) and (101) textures, respectively. Fig. 7 presents the microstructures of the mesh-type specimen, which exhibited an  $\alpha'$ -martensite microstructure with narrow laths. The  $\alpha'$ -martensite is more brittle than a Widmanstätten  $\alpha$ -lamellar structure; hence, the mesh-type specimen could have poor elongation properties compared to the solid type specimen.

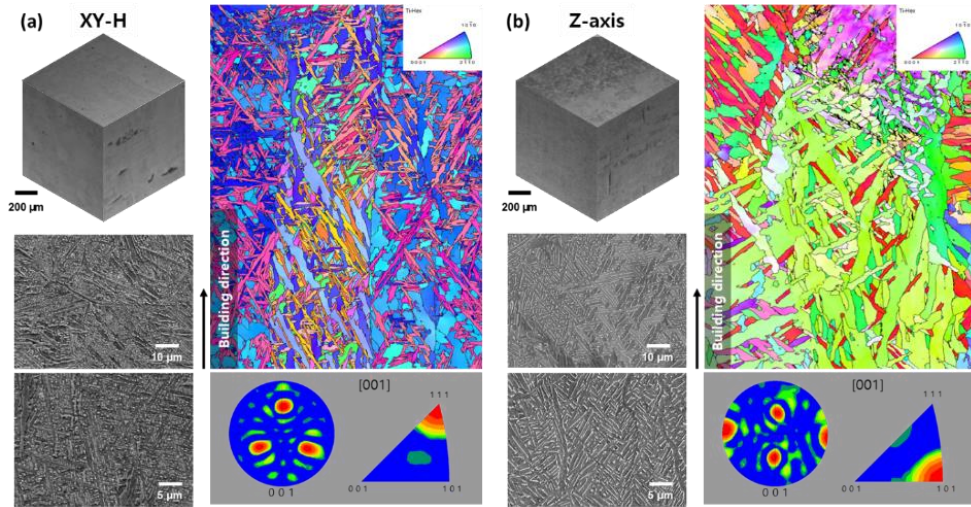


**Fig. 6** Solid tensile electron backscatter diffraction characterization of the specimen along the a XY-H axis and b Z-axis

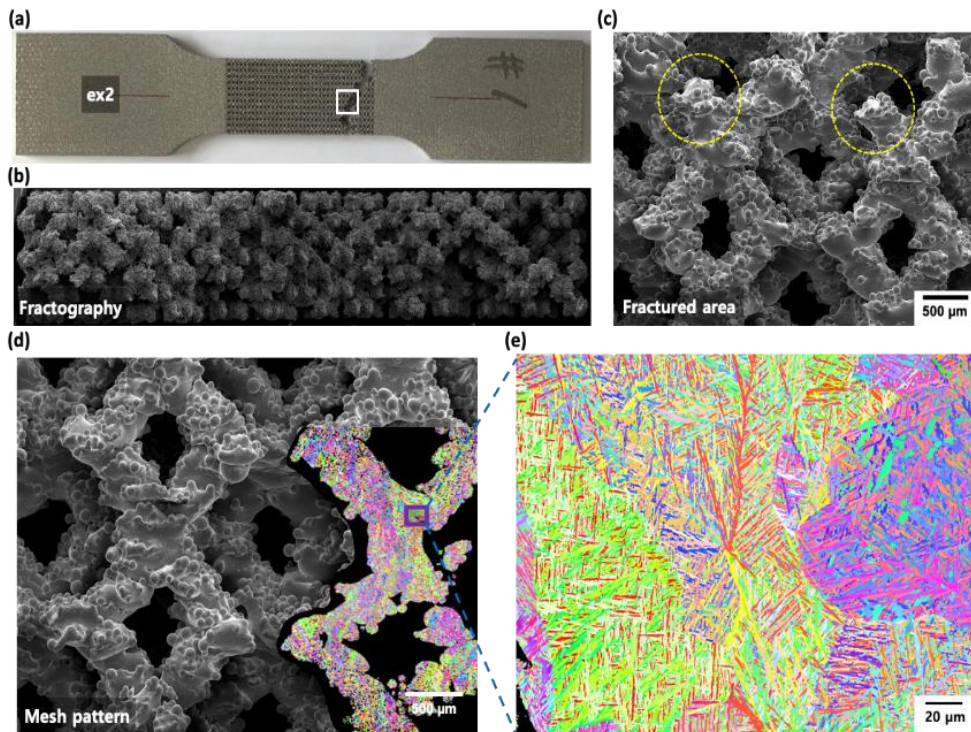


**Fig. 7** Microstructural analysis of the mesh structure of the tensile specimens. a Mesh-type tensile specimen, b Fractography of the mesh specimen, c Extended view of the fractured area, d EBSD-overlapped mesh structure, e Extended view of the EBSD of the mesh structure

– *Fractography of the tensile specimens*

To characterize the fracture behavior of Ti-6Al-4V, fractographical analysis was performed, as shown in Fig. 8. Tiny gas pores, which functioned as the crack initiation sites, were observed in the ductile ruptured area of the XY-H axis specimen (Fig. 8[a-1] and [a-3]). In the vicinity of the shear fractured area near the surface, pores and relatively large gas pores were observed, which decreased the tensile elongation (Fig. 8[a-2] and [a-4]). The initial voids were formed in the center of the specimen owing to the triaxial stress condition, and these voids later grew and coalesced to form a crack. Moreover, cracks originated from the cluster of unmelted powders, leading to unstable crack propagation (Fig. 8[b-4]). In addition, the specimen broke into irregular cup and cone shapes, and the location of the fracture was not constant. In the Z-axis specimen, a shear lip surrounded the entire specimen, whereas the shear lip was discontinuous in the XY-H specimen. Therefore, crack bursting occurred toward the surface of the specimen in the XY-H specimen, which decreased the tensile elongation.

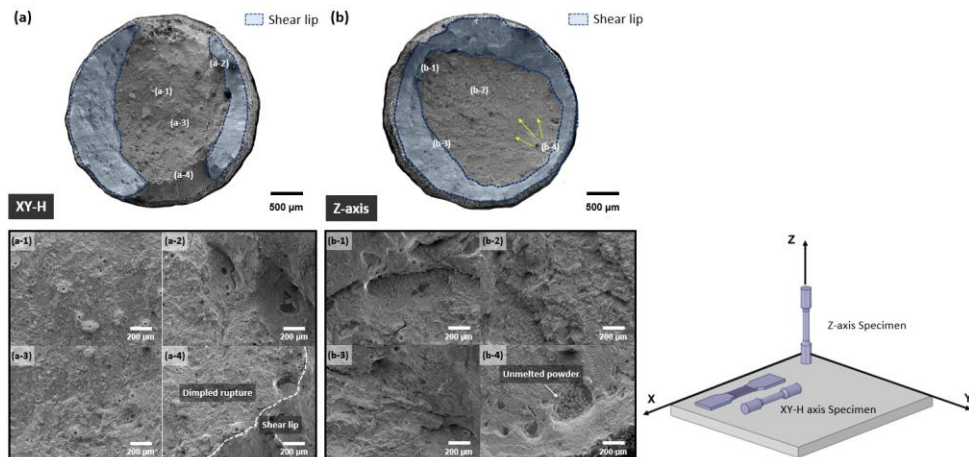


**Fig. 8** Fractography of the tensile test specimens. a XY-H axis, b Z-axis

– *Fractography of the fractured implant*

The proximal fractured part is shown in Fig. 4c with a note on the solid–mesh connection boundary and the center area. The solid–mesh boundary was observed through SEM (Fig. 9a), which clearly showed the detachment of the boundary mesh structure from the solid body. In Fig. 9b, the mesh fracture could be easily located on the center of the head. The solid structure of the boundary was fractured after elongation (Fig. 9a), but the mesh structure (Fig. 9b) was broken by brittleness. Moreover, there were unmelted powders throughout the whole fractured surface.

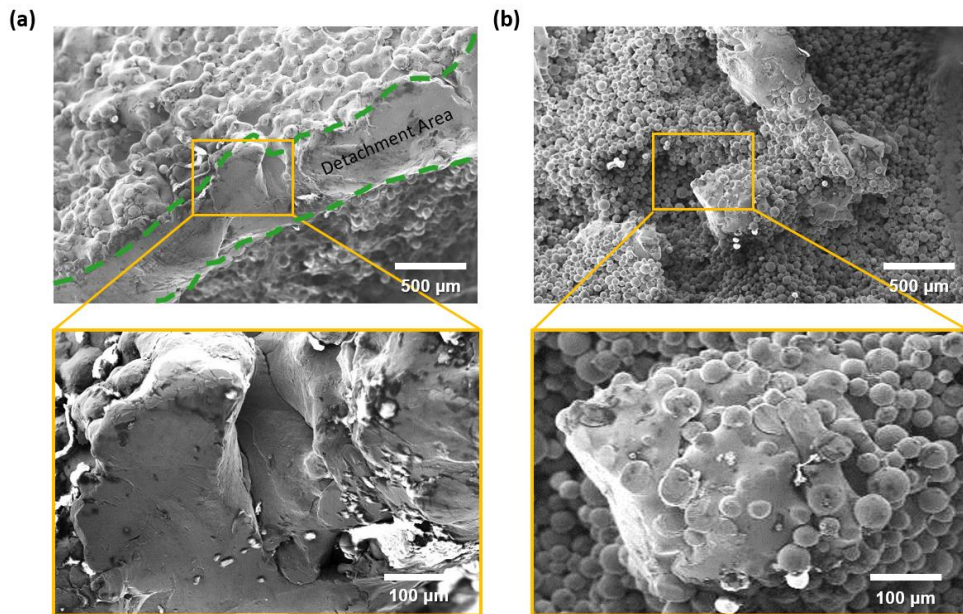


**Fig. 9** Scanning electron microscopy (SEM) of the fractured implant; a Boundary area, b Center area of mesh structure

– *Finite element analysis for the hybrid structure*

The solid–mesh hybrid structure was simulated under various conditions (Fig. 10). The relative length and cut surface area ratio between the solid and mesh structures were set as 1:2 and 20%–60%, respectively, as shown in Fig. 10a. The von Mises stress generally tended to concentrate on the boundary area of the solid and mesh structure, as shown in Fig. 10b. As seen in Fig. 10c, d, the axial load angle varied from  $0^\circ$  to  $90^\circ$  for each of the 20%, 40%, and 60% mesh cases. The maximum von Mises stress at the boundary of the mesh and solid structures for the 60% mesh case was relatively higher than that for the other cases for every force input angle. The maximum von Mises stress tended to saturate as the input force angle approached  $90^\circ$ . When the relative mesh length was doubled, this saturation behavior also appeared for the 20% mesh area case. However, the saturation behavior tended to disappear for the 40% and 60% mesh cases, which indicates that there is a certain mesh ratio where the maximum Von Mises stress does not reach an excessive value under high–angle force input.

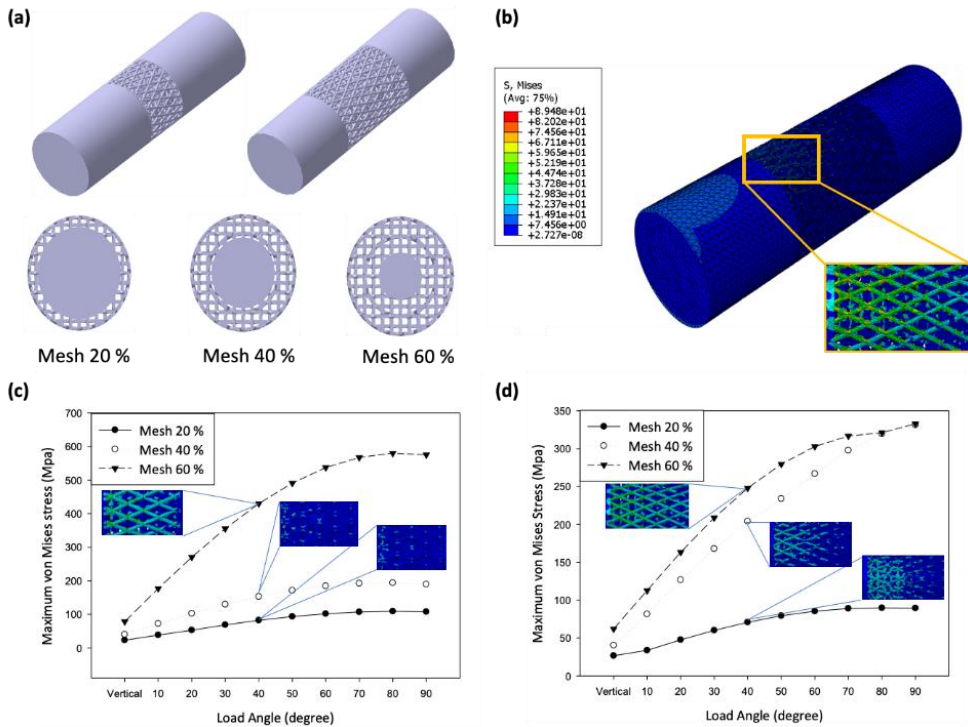


**Fig. 10** Finite element analysis (FEA) result for the mesh structure content and load angle. a Six types of 3D specimens were used in the FEA: 20 mm and 40 mm in length, with 20%, 40%, and 60% of mesh ratio. b One example of the FEA result. The stress was concentrated on the mesh structure of the central region. c Maximum von Mises stress according to the mesh structure contents and load angle of 500 N at 20 mm. d A 40–mm length

– *Finite element analysis for the fractured implant*

For further simulation with practical force input, the direction and amount of force were derived from a personalized body model using commercial software (AnyBody Modeling System, Denmark), as shown in Fig. 11c, d. The fast gait condition was simulated through FEA to examine the harshest environment for verifying the stability of the implant. In the FEA simulation, the distal femur was fixed, and external force was applied to the proximal femur head. Based on the actual physiological loading of the human body, two conditions were assumed: fast gait and limping gait, and two cases were considered for both conditions. The direction and force angle for the two conditions were based on the data obtained from the AnyBody Modeling System.

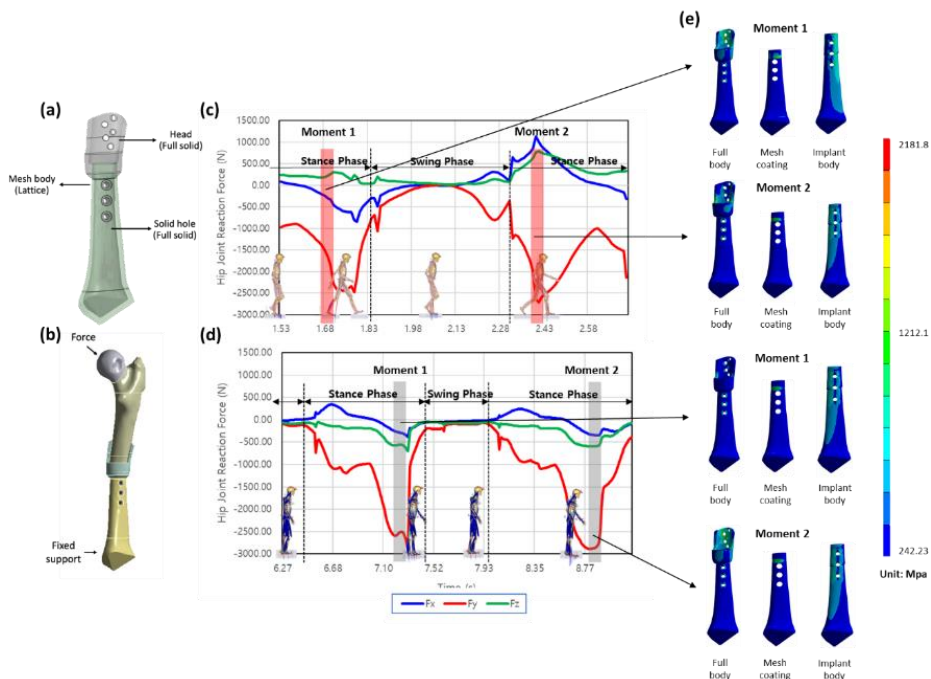


**Fig. 11** Configuration for computational analysis. a Implant composition for the input parameter in simulation. b Boundary condition in the finite element analysis (FEA). c–e Joint reaction force analysis; c Fast gait, d Limping gait, e FEA result for the implant

**Table 2.** Analysis results of right hip joint reaction

Type of gait	Time (s)	Force (N)		
		$F_x$	$F_y$	$F_z$
Fast 1	1.72	-516.26	-2406.36	302.08
Fast 2	2.41	1007.22	-2716.50	791.81
Limping 1	7.80	-379.53	-2884.16	-699.10
Limping 2	8.85	-347.42	-2860.48	-590.91

The input composition of the implants and the boundary condition for simulation is shown in Fig. 11a, b. The von Mises stress on three parts, namely the full body, mesh body, and solid hole, was simulated in the analysis, as shown in Fig. 11a. In Table 2, the maximum Von Mises stress in the fast gait 1 and 2 conditions was 1013.9 and 2030.8 MPa, respectively, and its value in the limping gait 1 and 2 conditions was 883.41 and 802.21 MPa, respectively. The largest von Mises stress corresponded to the fast gait 2 condition. Moreover, in this condition, the stress was 329.52 and 2000.4 MPa in the mesh body and solid hole, respectively. The stress was concentrated on the upper part of the mesh body, which formed the connection between the head and solid hole. Overall, the computational analysis indicated that the fracture of the implant was partly due to the physiological loading of the human body after ambulatory recovery without limping, and the stress was concentrated in the head-body connection.

### 1.3. Discussion

The 3D-printed customized Ti-6Al-4V implant is utilized as a treatment for bone malignancy to replace bone tissue and enhance the function of the affected extremity after limb salvage surgery. Down-sizing of the surgery with preservation of the normal adjacent joint is an important reason for considering limb salvage surgery using a 3D-printed implant. However, reliability of the implant has not been fully addressed. The mechanical behavior of the Ti-6Al-4V alloy varies according to fabrication conditions. Moreover, custom-made designs for 3D implants including a mesh structure should be confirmed by computational analysis because of the time limitation before application in cancer patients. In this study, in-depth mechanical and computational analysis for the fractured implant, which was used for a patient with chondrosarcoma in the femur, was conducted. Mechanical properties and microstructural features of the Ti-6Al-4V solid and mesh structures, which were fabricated by EBM 3D-printing, were obtained. FEA using the preceding experimental data worked well in predicting the specific fracture site and a fast, normal gait as the condition that was partially responsible for creating the implant fracture.

The comprehensive mechanical, microstructural, and computational analysis of the custom-made Ti-6Al-4V implant revealed that the in-situ fracture may have occurred mainly for the following two reasons: a microstructural aspect and an implant design. Despite the possibility of crack initiation due to unmelted metal powder, the solid Ti-6Al-4V had sufficient mechanical strength provided by a Widmanstätten  $\alpha$ -lamellar structure for long-term body weight tolerance. Conversely, the mesh Ti-6Al-4V had poor elongation characteristics with a brittle  $\alpha'$ -martensite microstructure featured by narrow laths. Excessive stress concentration was also detected near the brittle mesh and solid connection areas within the designed implant, which made the mesh structure unable to withstanding the physiological loading pattern of

human walking.

The results indicated that although the strength of the implants printed on the EBM 3D printer was sufficient, the model was poorly formed when the mesh structure was included. However, the mesh structure had unique advantages: provided a scaffold for bone ingrowth, a lightweight design, and reduced metal artifacts during postoperative surveillance for local recurrence [24,25]. Providing an appropriate pore structure is the most important consideration when using mesh structure to enhance osteointegration. A few animal studies reported the osteoinductive effect of the 3D-printed titanium alloy implant [30–34] and one human case study reported 8–10% of bone integration to the mesh structure [35]. The mesh structure was commonly mentioned in previous literature on 3D-printed custom-made implants in orthopedic oncology, especially bone and implant junction, as it provides a scaffold for bone ingrowth [25–27]. When a mesh structure is included in the implant, it is necessary to verify the design.

While these thorough simulations offer insight into the design of custom-made implants for bone cancer treatment, a pre-simulation big data platform is necessary for a quick assessment of designed implants prior to cancerous bone replacement surgery. In this study, FEA based on experimental mechanical properties showed promising predictive power for the verification of the custom-made implant design. Previous reports using FEA evaluated the mechanical behavior of 3D-printed custom-made implants [36, 37], but not all FEA were based on the experimental data of the 3D-printed metal. While these in-depth simulations should be performed prior to surgery, the time limitation of urgent cancer surgery may hinder sufficient simulations. Simply put, once bone cancer has been diagnosed, there is a strict time limitation for treatment; thus, lengthy, in-depth computer-aided engineering analyses, including human modeling and FEA, are not feasible. These limitations shall be addressed in our future work by obtaining a big data pre-simulation platform for most possible fractures of 3D-printed implants. Future research encompassing the

aforementioned pre-simulated big data platform should establish guidelines for mesh and solid structure designs that can withstand the physiological loading patterns of different patients to facilitate better surgical outcomes. In addition, the time required for analysis can be reduced to a few days by simplifying the analysis through the use of a standard human body model.

Another limitation of this study was that the analytic power of computer-aided mechanical analysis, including human modeling and FEA, was validated in only one representative case. Moreover, the final goal of computer-aided structural analysis is not postoperative evaluation, but preoperative performance prediction during the custom-made implant design process to improve the design through feedback. In this study, FEA predicted fracture conditions in a specific patient who suffered from an implant fracture. Although FEA showed promising results, it is difficult to determine whether this method has undergone sufficient verification. A 3D-printed custom-made implant is a highly variable and complicated mixed structure containing solid and mesh elements. Therefore, FEA must be applied for hybrid structures and real implants with the aim of compiling fundamental and clinical evidence before being used in patients. In conclusion, the FEA method for a custom-made implant design with a mesh structure should be further validated.

## Chapter 3. Conclusion

The results indicated that although the strength of the implants printed on the EBM 3D printer was sufficient, the model was poorly formed when the mesh structure was included. Therefore, the structural analysis is important to indicate weak point of the implant design. Considering the time constraints of bone cancer patients, the computer-aided engineering including a human body simulation and FEA was a feasible solution. FEA based on results of tensile experiments and human modeling was well predicted implant fracture, in the representative patient.

The final goal of this study is to improve implant design through feedback during the actual implant design process so that stable implants can be created and used for patients. To this end, it is necessary to simplify the method used in this study so that the analysis can be completed within a few days, and to confirm the usefulness of this method in more complex specimens and implants in the future.

# Bibliography

1. Mitchell A, Lafont U, Hołyńska M, Semprimoschnig C (2018) Additive manufacturing—a review of 4D printing and future applications. *Addit Manuf* 24: 606–626.
2. Bhavar V, Kattire P, Patil V et al (2014) A review on powder bed fusion technology of metal additive manufacturing. 4<sup>th</sup> Int Conf and Exhibition on Additive Manufacturing Technologies–AM–2014, pp 1–2
3. Froes F, Dutta B (2014) The additive manufacturing (AM) of titanium alloys. *Adv Mater Res* 1019: 19–25.
4. Liu A, Xue G, Sun M et al (2016) 3D printing surgical implants at the clinic: a experimental study on anterior cruciate ligament reconstruction. *Sci Rep* 6:21704.
5. Dawood A, Marti BM, Sauret–Jackson V (2015) 3D printing in dentistry. *Br Dent J* 219(11): 521–529.
6. Jung J, Lee J, Cho D (2016) Computer–aided multiple–head 3D printing system for printing of heterogeneous organ/tissue constructs. *Sci Rep* 6:21685.
7. Yang F, Chen C, Zhou Q et al (2017) Laser beam melting 3D printing of Ti6Al4V based porous structured dental implants: fabrication, biocompatibility analysis and photoelastic study.

Sci Rep 7: 45360.

8. Zhang B, Pei X, Zhou C et al (2018) The biomimetic design and 3D printing of customized mechanical properties porous Ti6Al4V scaffold for load-bearing bone reconstruction. *Mater Des* 152(15): 30–39.
9. Zhao L, Pei X, Jiang L et al (2019) Bionic design and 3D Printing of porous titanium alloy scaffolds for bone tissue repair. *Compos B Eng* 162:154–161.
10. Song P, Hu C, Pei X et al (2019) Dual modulation on crystallinity and macro/micro structures of 3D printed porous titanium implants to enhance the stability and osseointegration. *J Mater Chem B* 7(17): 2865–2877.
11. Pei X, Wu L, Zhou C et al (2021) 3D printed titanium scaffolds with homogeneous diamond-like structures mimicking that of the osteocyte microenvironment and its bone regeneration study. *Biofabrication* 13: 015008.
12. Lei H, Yi T, Fan H et al (2021) Customized additive manufacturing of porous Ti6Al4V scaffold with micro-topological structures to regulate cell behavior in bone tissue engineering. *Mater Sci Eng C Mater Bio Appl* 120: 111789.
13. Chen Y, Bian L, Zhou H et al (2010) Usefulness of three-dimensional printing of superior mesenteric vessels in right

- hemicolon cancer surgery. *Sci Rep* 10(1): 11660.
14. Guan B, Wang H, Xu R et al (2016) Establishing antibacterial multilayer films on the surface of direct metal laser sintered titanium primed with phase-transited lysozyme. *Sci Rep* 6: 36408.
  15. Yan L, Lim J, Lee J et al (2020) Finite element analysis of bone and implant stresses for customized 3D-printed orthopaedic implants in fracture fixation. *Med Biol Eng Comput* 58(5):921–931.
  16. Ma L, Zhou Y, Zhu Y et al (2017) 3D printed personalized titanium plates improve clinical outcome in microwave ablation of bone tumors around the knee. *Sci Rep* 7(1): 7626.
  17. Harrysson OLA, Cormier DR (2006) Advanced manufacturing technology for medical applications: reverse engineering, software conversion and rapid prototyping. In: Gibson I (ed) *Direct fabrication of custom orthopedic implants using electron beam melting technology*, pp 191–206
  18. Parthasarathy J, Starly B, Raman S et al (2010) Mechanical evaluation of porous titanium (Ti6Al4V) structures with electron beam melting (EBM). *J Mech Behav Biomed Mater* 3(3): 249–259
  19. Choy WJ, Mobbs RJ, Wilcox B et al (2017) Reconstruction of

- thoracic spine using a personalized 3D-printed vertebral body in adolescent with T9 primary bone tumor. *World Neurosurg* 105: 1032.e13–1032.e17.
20. Park JW, Kang HG, Lim KM et al (2018) Three-dimensionally printed personalized implant design and reconstructive surgery for a bone tumor of the calcaneus: a case report. *JBJS Case Connect* 8(2): e25.
  21. Kotz, R (1993) Tumor endoprosthesis in malignant bone tumors. *Der Orthop* 22(3): 160–166
  22. Kim Y, Jang WY, Park JW et al (2020) Transepiphyseal resection for osteosarcoma in patients with open physes using MRI assessment. *Bone Joint J* 102-B(6): 772–778
  23. Eleutério SJ, Senerchia AA, Almeida MT et al (2015) Osteosarcoma in patients younger than 12 years old without metastases have similar prognosis as adolescent and young adults. *Pediatr Blood Cancer* 62(7): 1209–1213.
  24. Park JW, Kang HG, Kim JH et al (2021) The application of 3D-printing technology in pelvic bone tumor surgery. *J Orthop Sci* 26(2): 276–283.
  25. Park JW, Kang HG, Kim JH et al (2020) New 3-dimensional implant application as an alternative to allograft in limb salvage surgery: a technical note on 10 cases. *Acta Orthop* 4:

489–496.

26. Angelini A, Trovarelli G, Berizzi A et al (2019) Three–dimension–printed custom–made prosthetic reconstructions: from revision surgery to oncologic reconstructions. *Int Orthop* 43(1): 123–132.
27. Liang H, Ji T, Zhang Y et al (2017) Reconstruction with 3D–printed pelvic endoprostheses after resection of a pelvic tumour. *Bone Joint J* 99–B(2): 267–275.
28. Tsuboyama T, Windhager R, Dock W et al (1993) Knee function after operation for malignancy of the distal femur: quadriceps muscle mass and knee extension strength in 21 patients with hinged endoprostheses. *Acta Orthop Scand* 64(6): 673–677.
29. Holm I, Nordsletten L, Steen H, et al (1994) Muscle function after mid–shaft femoral shortening. A prospective study with a two–year follow–up. *J Bone Joint Surg Br* 76(1): 143–146.
30. Mumith A, Coathup M, Chimutengwende–Gordon M et al (2017) Augmenting the osseointegration of endoprostheses using laser–sintered porous collars: An in vivo study. *Bone Jt J* 99: 276–282.
31. McGilvray KC, Easley J, Seim HB et al (2018) Bony ingrowth potential of 3D–printed porous titanium alloy: A direct

- comparison of interbody cage materials in an in vivo ovine lumbar fusion model. *Spine J* 18: 1250–1260.
32. Wu SH, Li Y, Zhang YQ et al (2013) Porous titanium–6 aluminum–4 vanadium cage has better osseointegration and less micromotion than a poly–ether–ether–ketone cage in sheep vertebral fusion. *Artif Organs* 37: E191–E201.
  33. Li JP, Habibovic P, van den Doel M et al (2007) Bone ingrowth in porous titanium implants produced by 3D fiber deposition. *Biomaterials* 28: 2810–2820.
  34. Michael DW, Simon Z, Jasmine R et al (2016) Influence of Microarchitecture on Osteoconduction and Mechanics of Porous Titanium Scaffolds Generated by Selective Laser Melting. *3D Print Addit Manuf* 3: 142–151.
  35. Park JW, Song CA, Kang HG et al (2020) Integration of a three–dimensional–printed titanium implant in human tissues: case study. *Applied Sciences* 10(2): 553.
  36. Park DW, Lim A, Park JW et al (2019) Biomechanical evaluation of a new fixation type in 3D–printed periacetabular implants using a finite element simulation. *Applied Sciences* 9(5): 820.
  37. Wong KC, Kumta SM, Geel NV et al (2015) One–step reconstruction with a 3D–printed, biomechanically evaluated

custom implant after complex pelvic tumor resection.

Computer Aided Surgery 20(1): 14–23.



# 초 록

서론:

사지 구제술로 통칭되는 수술은 골종양 치료에서 가장 핵심적인 과정이다. 골종양은 그 형태와 위치, 그리고 크기의 다양성으로 인하여 사지 구제술을 위한 종양 절제 후 환자마다 매우 다른 양상의 골결손이 남는다. 최근 정형외과 종양학에서 3D 프린팅 방법으로 제작한 환자 맞춤형 Ti-6Al-4V 재질의 임플란트를 사지 구제술에 사용한 후, 단기 추사에서 우수한 결과를 보였다는 연구가 보고되고 있다. 그러나 3D 프린팅 임플란트와 환자 맞춤형 디자인에 대한 실험적인 증거는 부족한 실정이다. 3D 프린팅이라는 새로운 방식으로 출력되는 임플란트의 성능 평가를 위하여, 생산된 금속체에 대해 기초실험으로서 인장 실험이 선행되어야 한다. 이로부터 얻은 데이터를 활용하여 컴퓨터 시뮬레이션을 수행하면, 환자 맞춤형 디자인 임플란트의 구조를 평가할 수 있다.

연구방법:

임플란트 파손을 경험한 실제 환자의 임플란트의 파손 분석을 금속 인장시험과 이를 활용한 컴퓨터 시뮬레이션으로 진행하였다. 먼저, 임플란트를 생산하는 것과 같은 조건으로 전자빔방식의 3D 프린터를 활용하여 인장 시편을 제작하였다. 인장 시편은 강체구조와 메쉬구조로 각각 제작하였으며, 이에 대한 인장시험을 수행하여 3D 프린팅된 금속체에 대한 물성치를 획득하였다. 아울러, 임플란트의 파손면과 3D 프린팅 인장시편의 파단면을 전자현미경으로 비교분석하였다. 이 데이터를 활용한 유한요소분석법을 통하여 임플란트의 구조와 성능을 분석하였다.

결과:

3D 프린팅된 Ti-6Al-4V 시편의 실험 결과 메쉬구조는 33-54 MPa, 강체구조는 976-1000 MPa의 항복강도를 보였다. 특히 메쉬구조에서는 연신률이 1% 미만으로 취성에 취약함을 보였다. 임플란트와 인장시편의 파단면 분석에서는 공통적으로 덜 용융된 금속파우더가 관찰되었다. 실험데이터를 대입한 인체모사구조를 통한 컴퓨터 시뮬레이션 임플란트 성능분석에서는 정상보행 조건에서 임플란트 상부의 취약점을 지적하였다.

**결론:**

전자빔 방식의 3D 프린터로 생산한 Ti6Al4V 금속의 물리적 성질은 전통적인 방식으로 생산한 것과 비교하여 정형외과 임플란트를 제작하기에 충분한 것으로 평가되었다. 선행 실험데이터를 대입한 컴퓨터 시뮬레이션을 통한 임플란트 성능 분석 결과는 임플란트 파단과 파단되는 상황을 잘 예측하였다. 본 연구에서 사용한 컴퓨터 시뮬레이션 기법을 통한 임플란트 성능 분석법을 일반화하고 간소화하기 위하여, 향후 다양한 임플란트에 본 방법론을 적용해 볼 필요가 있다.

**주요어 :** 육종, 골격계 암, 파단 분석, 3D 프린팅, 티타늄 합금 임플란트, 전자빔용융

**학 번 :** 2018-39923